Received: 16 October 2021 | Revised: 20 August 2022 | Accepted: 24 October 2022

DOI: 10.33012/navi.584

ORIGINAL ARTICLE

Extending the Real-Time Kinematics Survey Method to Global Navigation Satellite System-Denied Areas Using a Low-Cost Inertial-Aided Positioning Pole

Changxin Lai[1] | **Ruonan Guo**[2] | **Qijin Chen**[1] | **Xiaoji Niu**[1]

[1] GNSS Research Center, Wuhan University, China,

[2] School of Geodesy and Geomatics, Wuhan University, China,

Correspondence
Qijin Chen, GNSS Research Center of Wuhan University.
Email: chenqijin@whu.edu.cn

Abstract

The global navigation satellite system (GNSS) real-time kinematics (RTK) survey method cannot be used in GNSS-denied areas largely due to signal blockage. In this work, we aim to extend high-precision RTK positioning capability to GNSS-denied areas via post-processing using an inertial-aided positioning pole that contains a inexpensive inertial measurement unit (IMU) chip and an RTK receiver. The positioning accuracy can be maintained at an acceptable level by using the pole as a walking stick with the pole periodically landing on the ground. Because the pole tip velocity is zero when it maintains contact with solid ground, lever-arm compensated zero-velocity updates (LA-ZUPTs) can be used to suppress errors in the inertial navigation system (INS) in GNSS-denied areas. Experimental results reveal that this method can be used to bridge up to a 60-meter GNSS gap to maintain sub-decimeter-level survey accuracy.

Keywords

consumer-grade IMU, GNSS-denied positioning, inertial-aided positioning pole, RTK survey, zero velocity update

1 | INTRODUCTION

With the development of global navigation satellite systems (GNSSs) and continuously operating reference stations (CORSs), real-time kinematics (RTK) has emerged as a high-precision positioning technique that can be applied widely in various positioning, navigation, and timing applications (Hein, 2020). RTK positioning is quite popular in the surveying market and is generally accepted as a powerful surveying method. The typical RTK survey instrument is a two-meter-high pole with a GNSS receiver at the top and a spike at the bottom. The instrument is placed vertically on the target point and its position is obtained by reducing the offset between the antenna phase center (APC) and the pole tip. However, the satellite signal may be reflected or blocked by obstacles such as high walls, buildings, and dense tree canopies that are frequently found in complex environments. These challenging environments can induce multipath effects and limit the number of visible satellites, thereby resulting in the degradation of RTK positioning signal. In the worst-case situation, known

as a GNSS outage or a GNSS-denied scenario, GNSS signals are completely unavailable. This may occur inside or between buildings or in a heavily-forested area. RTK positioning is not available in these situations and it thus becomes difficult to obtain accurate and reliable positioning results of targets in surveying (Teunissen & Montenbruck, 2017).

While the total station can be used to measure the position of a target in a GNSS-denied area, the use of this traditional high-precision surveying instrument requires the targets to be visible to one another and involves time-consuming operations. In recent years, information from integrated INS/GNSS navigation systems has led to the development of tilted RTK with low-cost inertial measurement units (IMUs) and advanced signal-tracking technologies. Tilted RTK utilizes the attitudes provided by the RTK-aided inertial navigation system (INS) initial alignment solutions to obtain pole tip positioning with tilt compensation. Therefore, the applicability of high-precision RTK positioning can be extended to some otherwise-restricted environments (Luo et al., 2018). For example, the range of RTK-fixed solutions may increase by tilting the pole to increase the distance from the antenna to the building or wall and thus obtain more visible satellites and reduced multipath interference. While tilting the pole can address some of the disadvantages of partially-sheltered conditions that limit RTK positioning, this method remains incapable of handling GNSS-denied environments, including areas that are inside buildings, under bridges, or heavily forested. With the rapid development of microelectromechanical system (MEMS) IMUs, diversified product series now provide low-cost MEMS IMU modules and even chips with considerable precision and significant potential for use in these measurements (El-Sheimy & Youssef, 2020). Therefore, MEMS-based inertial navigation systems (INSs) that provide high-frequency smoothed and high-precision navigation information detailing position, velocity, and attitude with significant precision when aided by external information to reduce rapid drift, have been used widely in various applications in navigation and engineering surveys (Schwarz, 1983), such as railway track (Chen et al., 2018; Chen et al., 2015; Gao et al., 2018) and pipeline surveying (Chen et al., 2019; Chowdhury & Abdel-Hafez, 2016; Guan et al., 2020). Here, we aimed to determine whether it might be possible to utilize a low-cost MEMS IMU to extend the positioning capability of the RTK survey instrument to GNSS-denied areas.

Inspired by the indoor pedestrian dead-reckoning navigator that uses a foot-mounted INS with zero-velocity updates (ZUPTs) available periodically for each step to correct the velocity error (Feliz Alonso et al., 2009; Foxlin, 2005; Niu et al., 2019; Ren et al., 2016), we mounted a low-cost IMU on the pole tip and operated the pole as a walking stick. In this way, the device can utilize the periodic ZUPTs when the pole tip lands on the ground at or after each step. A typical walking-stick-like manipulation includes two different dynamic phases (Figure 1). The first is the flying phase when the pole tip is not in contact with the ground; the second is the landing phase when the pole tip lands on the ground and the pole body rotates around the pole tip. These two stages alternate repeatedly when walking from the fixed-RTK area to a GNSS-denied target point; regular zero-velocity observations at the pole tip are available to restrict low-cost INS drift over time and/or distance. ZUPT-aided INS has a much slower positioning drift and can extend the capability of the RTK survey during GNSS outages and obtain the coordinates of target points in GNSS-denied areas. Of note, the IMU does not have to be physically mounted on the pole tip. The IMU can be mounted anywhere on the pole and projected to the tip through lever-arm compensation to conduct the ZUPT; this is known as lever-arm compensated ZUPT (LA-ZUPT).

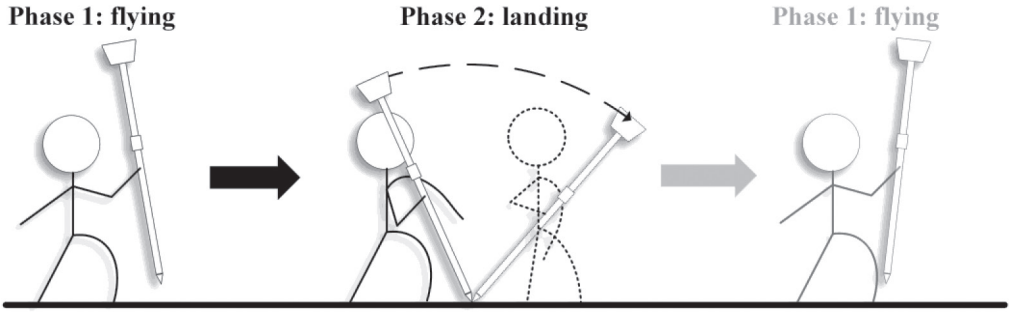

FIGURE 1 Illustration of the typical motion of the positioning pole manipulated as a walking stick. In phase 2, the pole tip maintains contact with the solid ground with a velocity of zero.

Unlike traditional ZUPT in which the entire carrier, including the IMU, needs to remain stationary, LA-ZUPT can register a velocity update using zero velocity observations at any known point of a rigid body with a fully-restrained connection to the IMU, regardless of its motion. We have named this RTK extension solution as INS/RTK with LA-ZUPT in this study. Correspondingly, the pole used to extend RTK positioning to GNSS-denied areas has been named the inertial-aided positioning pole. A similar idea has been included in two patent applications: *Walking Stick Navigator for Position Determination* and *AINS Enhanced Survey Instrument*, with a ZUPT-aided tactical grade IMU mounted at the bottom of the pole (Scherzinger, 2005, 2009). However, the device featured in these patent applications requires the use of a customized pole with the IMU at the bottom. Likewise, tactical grade IMU used to create this device may be too expensive for routine RTK survey instruments. By contrast, our study features a low-cost navigation solution with an inexpensive MEMS IMU chip mounted at a distance from the bottom of the pole that permits us to explore other possibilities for flexible installation and acceptable cost.

Given that post-processing can be applied to the INS/RTK with LA-ZUPT solution, the surveyor is required to ensure that the INS is fully initialized with RTK positioning at the beginning and is accurately corrected by RTK positioning after walking through the GNSS-denied area to reach an end spot under the open sky. In addition, as noted above, the pole must be manipulated as a walking stick while in transit through GNSS-denied regions to facilitate LA-ZUPT for the pole-mounted INS when the tip comes into contact with the solid ground. The INS-based extended Kalman filter (EKF) is selected as the optimal estimator and data processing algorithm, in terms of navigation states, including position, velocity, and attitude, as it fuses the INS with RTK positioning or zero-velocity measurement at the pole tip. Furthermore, Rauch-Tung-Striebel (RTS) smoothing for postprocessing was adopted to reduce the error of the INS even further which will ensure the reliable positioning capabilities of the inertial-aided positioning pole. The use of INS aided by regular LA-ZUPT during GNSS outages should generate much more accurate results than could be obtained with straightforward INS.

The remaining sections of this paper are organized as follows: Section 2 presents the workflow and algorithm of the proposed RTK extension solution together with a straightforward theoretical analysis. The information presented in Section 3 validates the feasibility of the proposed solution with multiple field tests including several experiments that were conducted to collect a sufficient number of samples. The performance and analysis of the results are reviewed from several different perspectives. Section 4 presents our conclusions.

2 | METHODOLOGY

The proposed method aims to extend RTK positioning capabilities to GNSS-denied regions using an inertial-aided positioning pole. To achieve the desired positioning accuracy, the typical surveying workflow was designed as follows:

1) Initially, the pole needs to be manipulated with sufficient movements in an open-sky environment. This will initialize the INS with the aid of RTK positioning before entering into a GNSS-denied area. Results from our previous research (Chen et al., 2020) suggest that rapid and accurate heading alignment can be achieved in a comparatively short time.
2) While moving along the survey trajectory into the GNSS-denied area, the pole is manipulated as a walking stick. The pole tip is then placed exactly on the target point to be surveyed and held stationary for some time so that the survey can be performed.
3) Step 2 is repeated at the next point of interest until an open-sky area is reached. The pole is manipulated with sufficient movements again until the end of the survey trajectory has been reached.
4) The survey trajectory can be reversed if necessary by returning to the starting point.

The algorithm used for the RTK extension solution is shown in Figure 2. In the first step, the aided INS requires initialization of the initial position, velocity, and attitude. The initial position and velocity of the INS are easily provided by the GNSS RTK receiver in an open-sky environment and coarse attitude initialization (i.e., coarse alignment) is performed by the accelerometer leveling process as well as the heading alignment method associated specifically with the low-cost MEMS IMUs (Chen et al., 2020). In the next step, the inertial navigation algorithm is executed. Additionally, the INS-based extended Kalman filter works by integrating the INS navigation states with available external information, including the RTK positioning results and the aforementioned zero-velocity observations at the pole tip which will correct the INS and restrict its drift. In addition to filtering, an RTS smoother is applied in post-processing to generate the globally optimal estimation of the INS error states, thereby further improving the INS precision. Finally, utilizing the corrected position and attitude of the INS as well as the lever-arm (LA) information,

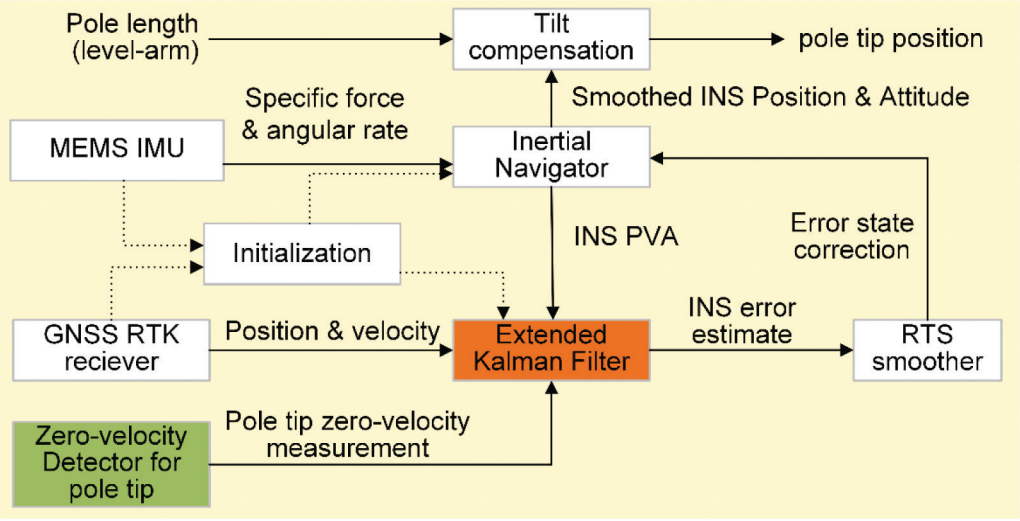

FIGURE 2 Basic schematic of the algorithm for the proposed RTK extension solution

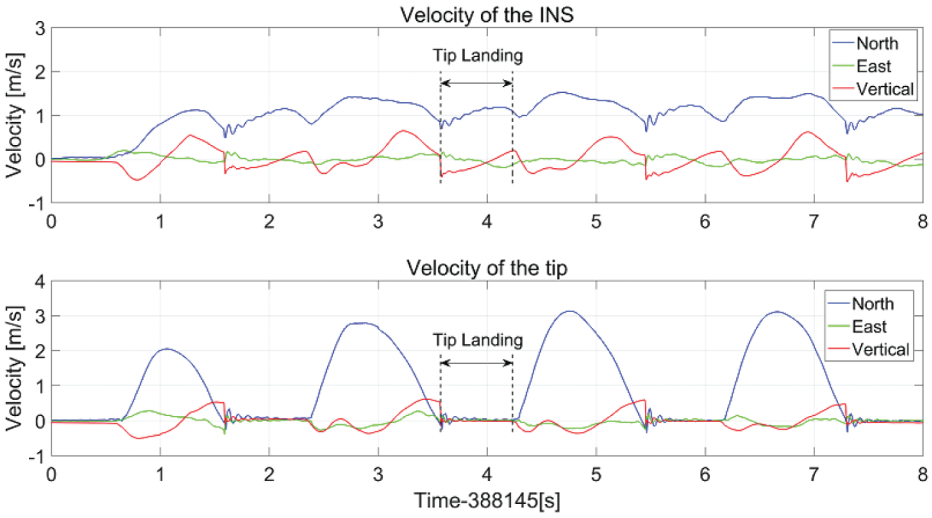

FIGURE 3 Comparison of the velocity of INS and the pole tip when the pole is manipulated as a walking stick. Note that the pole tip landing on the ground is nearly stationary, while the INS mounted on the middle of the pole keeps moving.

the coordinate of the pole tip landing on the target point is obtained by lever-arm compensation (Luo et al., 2018).

The algorithm of the RTK extension solution described above utilizes the pole tip zero-velocity to perform LA-ZUPT in EKF to estimate the INS error states and provide corrections to the INS during GNSS outages. As shown in Figure 3, the velocity of the pole tip is calculated from the INS-indicated velocity with lever-arm compensation. When the tip lands, its velocity is nearly zero even though the IMU that is fixed in the middle of the pole continues to move. Thus, LA-ZUPT is feasible and applicable in this case. LA-ZUPT extends the applicability of conventional ZUPT and provides a more flexible utilization strategy.

2.1 | Implementation of the EKF and RTS

The details regarding the implementation of the INS mechanization and the EKF specification for low-cost IMUs were described by Shin (2005). As long as the coarse initialization of the INS is complete, the INS-based EKF will work with the INS to provide error estimation aided by external observations such as RTK positioning and pole tip zero-velocity. With a fine implementation of an EKF with respect to the system and measurement models, the INS will identify an appropriate correction and generate a controlled system with closed-loop feedback (Maybeck, 1979).

2.1.1 | System Model

Given the low-cost MEMS chip and high dynamics of the pole that is manipulated as a walking stick, the INS error state vector of 21 dimensions in total was selected; this consists of a basic nine-dimensional navigation state error vector that includes position, velocity, and attitude errors. This is in addition to the 12-dimensional residual IMU error vector that includes residual biases and scale factor errors of the gyroscopes and accelerometers; the vector was defined as shown in Equation (1):

$$x = \left[\left(\delta r^n_{INS} \right)^T \left(\delta v^n_{INS} \right)^T \phi^T \;\; b_g{}^T \;\; b_a{}^T \;\; s_g{}^T \;\; s_a{}^T \right]^T \tag{1}$$

where the operator δ denotes the error of a variable, which means that δr^n_{INS} and δv^n_{INS} are the errors of position and velocity of the INS in the navigation frame (n-frame), respectively; ϕ is the attitude error defined in the phi angle model; b_g and s_g are the residual bias and scale factor errors of the gyroscopes, respectively; and b_a and s_a are the residual bias and scale factor errors of the accelerometers, respectively. Next, the overall system model in the continuous time form is expressed as shown in Equation (2):

$$\dot{x}(t) = \mathbf{F}(t)x(t) + \mathbf{G}(t)w(t) \tag{2}$$

where $\mathbf{F}(t)$ is the system matrix describing the system dynamics, $\mathbf{G}(t)$ is the system noise distribution matrix and $w(t)$ is the system noise vector. To implement the system model, the time derivative of each state variable must be calculated. The perturbation of the position, velocity, and attitude can be developed as shown in Figure 3 (Shin, 2005):

$$\begin{aligned} \delta\dot{r}^n &= -\omega^n_{en} \times \delta r^n + \delta\theta \times v^n + \delta v^n \\ \delta\dot{v}^n &= \mathbf{C}^n_b \delta f^b + \mathbf{C}^n_b f^b \times \phi - \left(2\omega^n_{ie} + \omega^n_{en}\right) \times \delta v^n \\ &\quad + v^n \times \left(2\delta\omega^n_{ie} + \delta\omega^n_{en}\right) + \delta g^n_b \\ \dot{\phi} &= -\omega^n_{in} \times \phi + \delta\omega^n_{in} - \mathbf{C}^n_b \delta\omega^b_{ib} \end{aligned} \tag{3}$$

where $\delta\theta$ is a rotation vector describing the misalignment of the computer frame with respect to the true n-frame; f^b is the specific force measured by the accelerometer and δf^b is its error; ω^n_{ie} is the angular rate of the Earth-centered Earth-fixed (ECEF) frame (e-frame) relative to the inertial frame (i-frame) in the n-frame and ω^n_{en} is the angular rate of the n-frame relative to the e-frame in the n-frame; $\delta\omega^n_{ie}$ and $\delta\omega^n_{en}$ are the errors of ω^n_{ie} and ω^n_{en}, respectively; δg^n_b is the error of local gravity of the IMU body frame (b-frame) in the n-frame; and ω^n_{in} is the angular velocity vector, where $\omega^n_{in} = \omega^n_{ie} + \omega^n_{en}$ and $\delta\omega^n_{in}$ is its corresponding error. The INS error parameters, i.e., b_g, b_a, s_g, and s_a, are modeled by the first-order Gauss–Markov process as shown in Equation (4):

$$\dot{x}_{GM}(t) = -\frac{1}{T_C} * x_{GM}(t) + w_{GM}(t) \tag{4}$$

where T_C is the correlation time of the process and $w_{GM}(t)$ is the driving white noise process. We refer the reader to the work of Maybeck (1979) for more details regarding this stochastic process. Furthermore, the discrete system model, which is widely used, can be expressed as shown in Equation (5):

$$x_{k+1/k} = \Phi_{k+1/k} * x_k + w_k \tag{5}$$

where Φ is the state transition matrix and w is the process noise of the discrete system. These are given as shown in Equation (6) and Equation (7):

$$\Phi_{k+1/k} = \exp\left(\int_{t_k}^{t_{k+1}} \mathbf{F}(\tau)d\tau\right) \approx \mathbf{I} + \mathbf{F}\left(t_k\right)\Delta t \tag{6}$$

$$w_k = \int_{t_k}^{t_{k+1}} \Phi(t_{k+1}, \tau)\mathbf{G}(\tau)w(\tau)d\tau \tag{7}$$

2.1.2 | Measurement Model

In the modified EKF, pole tip zero-velocity and RTK position observations are utilized to determine the LA-ZUPT and coordinate update (CUPT), respectively. The overall system measurement model is denoted as shown in Equation (8):

$$z = \mathbf{H}x + n_v \tag{8}$$

where z is the measurement vector containing information on the velocity measurement and position measurement; $\mathbf{H}$ is the design matrix; x is the aforementioned error state vector of the INS; and n_v is the measurement noise. The velocity measurement equation can be expressed as shown in Equation (9):

$$z_{ZUPT} = \hat{v}_{tip} - \tilde{v}_{tip} = \mathbf{H}_{ZUPT}x + n_v \tag{9}$$

where $\tilde{v}_{tip}$ is the virtually "measured" zero velocity at the pole tip, with $\tilde{v}_{tip} = [000]^T + n_{vT}$, and $\hat{v}_{tip}$ is the INS-indicated velocity at the pole tip obtained by velocity lever-arm compensation, as indicated in Equation (10):

$$\hat{v}^n_{tip} = \hat{v}^n_{INS} + \hat{\boldsymbol{C}}^{\boldsymbol{n}}_{\boldsymbol{b}}\left(\hat{\omega}^b_{eb} \times l^b_{tip}\right) = \hat{v}^n_{INS} - \left(\omega^n_{ie}\times\right)\hat{\boldsymbol{C}}^{\boldsymbol{n}}_{\boldsymbol{b}} l^b_{tip} - \hat{\boldsymbol{C}}^{\boldsymbol{n}}_{\boldsymbol{b}}\left(l^b_{tip}\times\right)\hat{\omega}^b_{ib} \tag{10}$$

where $\hat{v}^n_{INS}$ is the INS velocity; l^b_{bT} is the lever arm from the INS to the pole tip b-frame; $\hat{\omega}^b_{eb}$ is the angular rate of the e-frame relative to the b-frame in the b-frame, which can be separated into the angular rate of the e-frame relative to the inertial frame (i-frame) in the b-frame, $\hat{\omega}^b_{ie}$, and the angular rate measured by the gyroscope measurement, $\hat{\omega}^b_{ib}$. In addition, the perturbation model of $\hat{v}^n_{tip}$ can be obtained by perturbing the INS velocity $\hat{v}^n_{INS}$, rotation matrix $\hat{C}^n_b$ and gyroscope measurement $\hat{\omega}^b_{ib}$, assuming that l^b_{tip} is known precisely, as shown in Equation (11):

$$\delta\hat{v}^n_{tip} = \delta v^n_{INS} - \left(\left(\omega^n_{ie}\times\right)\left[\left(\boldsymbol{C}^{\boldsymbol{n}}_{\boldsymbol{b}} l^b_{tip}\right)\times\right] + \left[\boldsymbol{C}^{\boldsymbol{n}}_{\boldsymbol{b}}\left(l^b_{tip}\times\omega^b_{ib}\right)\times\right]\right)\boldsymbol{\phi} - \boldsymbol{C}^{\boldsymbol{n}}_{\boldsymbol{b}}\left(l^b_{tip}\times\right)\delta\omega^b_{ib} \tag{11}$$

The design matrix $\mathbf{H}_{ZUPT}$ can then be denoted as shown in Equation (12):

$$\mathbf{H}_{ZUPT} = \left[\mathbf{0}_3\ \mathbf{I}_3\ \mathbf{H}_{Z1}\ -\mathbf{C}^n_b\left(l^b_{tip}\times\right)\ \mathbf{0}_3\ \mathbf{H}_{Z2}\ \mathbf{0}_3\right] \tag{12}$$

where $\mathbf{I}_3$ and $\mathbf{0}_3$ denote the 3×3 identity and zero matrices, respectively; and $\mathbf{H}_{Z1}$ and $\mathbf{H}_{Z2}$ are 3×3 matrices that are given by:

$$\begin{cases} \mathbf{H}_{Z1} = -\left(\omega^n_{ie}\times\right)\left[\left(\mathbf{C}^n_b l^b_{tip}\right)\times\right] - \left\{\left[\mathbf{C}^n_b\left(l^b_p\times\right)\omega^b_{ib}\right]\times\right\} \\ \mathbf{H}_{Z2} = -\mathbf{C}^n_b\left(l^b_{tip}\times\right)diag\left(\omega^b_{ib}\right) \end{cases}$$

Similarly, for position measurements from the RTK receiver that are used for CUPT in the EKF, the position measurement can be expressed as shown in Equation (13):

$$z_{CUPT} = \mathbf{D}_R\left(\hat{r}^e_{GNSS} - r^e_{GNSS}\right) = \mathbf{H}_{CUPT}x + n_r \tag{13}$$

where $\hat{r}^e_{GNSS}$ and r^e_{GNSS} are the coordinates (latitude φ, longitude λ, and height h) of the INS-indicated position at the GNSS receiver's APC and the GNSS RTK

positioning result at the APC, respectively; $\mathbf{D}_R = diag(R_M + h,\ (R_N + h)cos\varphi,\ -1)$, where R_M and R_N are the radius of the meridian circle and the radius of the prime vertical, respectively. Thus, the design matrix $\mathbf{H}_{CUPT}$ can be denoted as shown in Equation (14):

$$\mathbf{H}_{CUPT} = \left[\mathbf{I}_3\ \mathbf{0}_3\ \left(\mathbf{C}_b^n l_{tip}^b\right)\times\ \mathbf{0}_3\ \mathbf{0}_3\ \mathbf{0}_3\ \mathbf{0}_3\right] \tag{14}$$

The statistical model that considers measurement noise has a significant influence on the Kalman filter algorithm for the optimal estimation of the system states. For CUPT, the standard deviation (SD) of the GNSS position measurement noise can be easily obtained from the SD of RTK positioning; however, for ZUPT, the determination of the SD is more difficult in theory. In this paper, we empirically tune the optimal SD by trial and error by considering the root-mean-square error (RMSE) of the positioning errors from multiple tests. The final optimal SD of the virtual zero-velocity observation errors is set at 0.06 m/s.

2.1.3 | *RTS Smoothing*

After the final CUPT in an open-sky area, a smoothing algorithm can be applied in post-processing to identify the global optimal estimated error states and thus improve the overall positioning accuracy by performing corrections to the INS. In this paper, we apply the RTS algorithm which is a well-known fixed-interval smoother. The RTS algorithm is relatively simple to implement and does not require the application of a full-scale backward filter. Further details of the algorithm can be found in the literature (Maybeck, 1979; Rauch et al., 1965). The principle is as shown in Equation (15) and Equation (16):

$$\hat{x}_{k/N} = \hat{x}_{k/k} + \mathbf{D}_k\left(\hat{x}_{k+1/N} - \hat{x}_{k+1/k}\right) \tag{15}$$

$$\mathbf{P}_{k/N} = \mathbf{P}_{k/k} + \mathbf{D}_k\left(\mathbf{P}_{k+1/N} - \mathbf{P}_{k+1/k}\right)\mathbf{D}_k^T \tag{16}$$

where the smoothing gain matrix $\mathbf{D}_k$ can be denoted as shown in Equation (17):

$$\mathbf{D}_k = \mathbf{P}_{k/k}\mathbf{\Phi}_k^T\mathbf{P}_{k+1/k}^{-1} \tag{17}$$

2.2 | Error State Observability

Although the EKF and RTS are expected to reduce the INS error to a large extent, the observability properties of the system error state affected by system dynamics will limit the performance of both the EKF and RTS. Using GNSS/INS integration as an example, if the carrier is moving without changes in acceleration and the gyro is low-grade, the component of the gyro bias in the direction of the specific force is unobservable; thus, the heading error can increase significantly and quickly over time (Hong et al., 2005).

Regarding the error state observability of the INS at the pole, the position, velocity, and horizontal attitude error are considered to be observable to some extent with the assistance of RTK positioning in an open-sky area. In addition, the velocity and horizontal attitude error are considered to be fully observable when aided by LA-ZUPT in GNSS-denied areas. However, the heading error may be unobservable

by CUPT for RTK positioning without proper maneuvering to generate acceleration changes; this will result in poor long-term navigation performance. In addition, when RTK positioning updates are unavailable in GNSS-denied environments, the position error will not be observable by LA-ZUPT. Furthermore, the position error may drift quickly without LA-ZUPT and CUPT during the pole flying phase (i.e., Phase 1 in Figure 1) in GNSS-denied environments.

Considering the restricted observability properties of the aided INS, the heading and positioning errors are sensitive to INS initialization, particularly with respect to the heading alignment. Consequently, it is necessary to initialize the INS completely at the beginning of the procedure and obtain sufficient EKF convergence after the GNSS outage at its end with the assistance of RTK positioning. It is also vital to apply RTS smoothing that utilizes the available RTK position and the heading constraint on both sides of the GNSS outage as this will provide a better estimate of the unobservable INS error states. This will lead to improved positioning of the target points, particularly because they may be located in the middle of the GNSS-denied area. From a spatial optimization point of view, the starting point and the endpoint should be located on different sides of the target point if feasible to obtain the best geometric constraint for the application scenario. In addition to the forward survey trajectory, a return trajectory can be added to counteract any position measurement errors related to heading errors and further improve the accuracy and robustness of surveying to the target point.

3 | EXPERIMENTS AND RESULTS

3.1 | Experiment Description

Field tests were conducted on a campus playground in open-sky conditions to validate the feasibility and performance of the proposed solution for extending the RTK positioning capability to GNSS-denied areas. The choice of the open-sky condition is reasonable because it ensures good observation conditions for the GNSS RTK. The open-sky condition is favorable for obtaining the ground truth using the integrated GNSS/INS reference system and also for identifying the reference truth coordinates of the target points measured accurately by a traditional RTK survey in advance. The GNSS-denied cases were simulated by manually discarding the RTK positioning update in subsequent aided INS data processing.

Datasets were collected using the assembled pole shown in Figure 4a, which has a GNSS antenna mounted at the top end, a MEMS INS/GNSS integrated system on an aluminum plate mounted in the middle of the pole, and a mechanical trigger mounted at the bottom tip. A quasi-tactical grade INS/RTK system was also attached to the aluminum plate to provide a reference truth for navigation information. The MEMS INS/GNSS integrated system used in the experiment is *INS-Probe* which was developed by the *i2Nav Group* of the *GNSS Research Center at Wuhan University* and uses a low-cost MEMS IMU chip, specifically, the ICM-20602 from *InvenSense*. The mechanical trigger connected to and synchronized with the *INS-Probe* was responsible for accurate detection when the pole tip was in contact with the solid ground. In this case, the switch is toggled on when the pole tip hits the ground and is toggled off once it has been lifted off, as shown in Figure 4b. The specifications of the instrument are as follows:

- IMU (embedded in the *INS-Probe*): *InvenSense ICM-20602*, an inexpensive MEMS IMU chip with gyroscope noise of $0.24\,\mathrm{deg}/\sqrt{h}$ and accelerometer noise of $100\,\mu\mathrm{g}/\sqrt{Hz}$, sampling at 200 Hz.

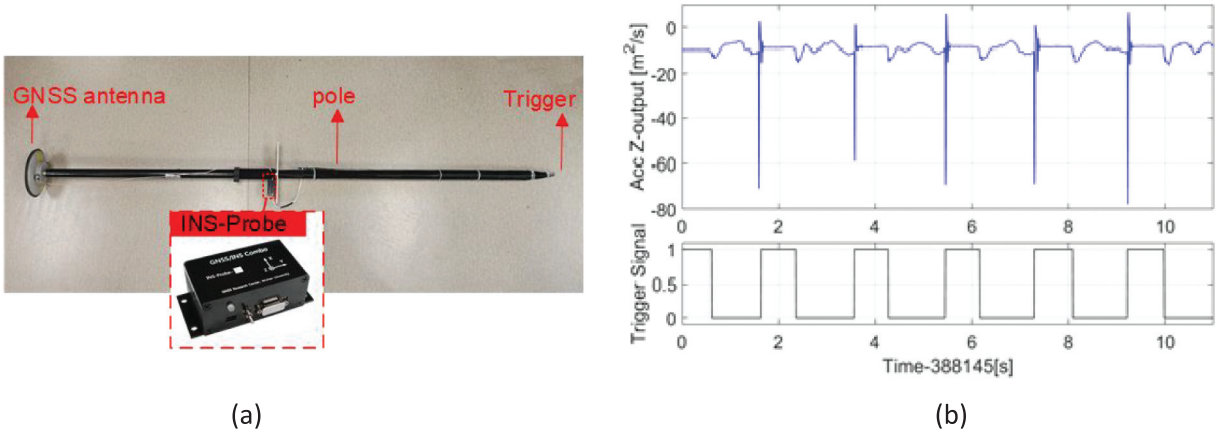

FIGURE 4 The inertial-aided positioning pole with a trigger that detects ground contact

- Trigger: A mechanical switch serving as the pole tip zero-velocity detector.
- GNSS receiver: Two *NovAtel OEM719D* GNSS receivers serve as the rover and base station for the RTK.
- GNSS antenna: A *NovAtel GPS-7-2GGL* antenna and a u-blox ANN-MB multiband GNSS antenna.
- INS/RTK reference system: A quasi-tactical IMU module and u-blox GNSS module that provide position reference at the centimeter level and heading reference accurate to 0.2° in the post-processing mode.

As described in Section 2.2, the straight-line trajectory (i.e., "I" shape) is the best trajectory for obtaining an accurate result under the constraints provided by the high-quality positioning result at the beginning and ending points outside of the GNSS-denied area. In addition, a shorter trajectory through the GNSS-denied area is favorable for obtaining a better positioning result. In reality, the GNSS-accessible spots near the target point will vary greatly with respect to distance and distribution. The three typical classes of trajectories (i.e., "I"-shaped, "L"-shaped, and "U"-shaped trajectories) and the I-shaped trajectory with the GNSS gap length varying from 100 m to 20 m were investigated individually. The designed trajectories with different distances are illustrated in Figure 5. In this study, the GNSS gap length refers to the length of the trajectory through the simulated GNSS-denied area; the effective RTK extension distance is half the GNSS gap length. The target point is set at a point in the center of the trajectory through the GNSS-denied area that is at the greatest distance to the GNSS-friendly spots on both sides and is likely to benefit the least from RTK positioning by RTS smoothing (i.e., a worst-case scenario).

In accordance with the survey workflow, the datasets were collected based on the following procedures: 1) Initialize the INS with sufficient movement of the pole at the starting point. 2) Walk along the designed trajectory toward the target point, manipulating the pole as a walking stick as though one was in a GNSS-denied environment while controlling the flying phase of the pole to be as brief as possible for better performance. (NB: We did this by walking rapidly with small steps so that the duration of the flying phase was approximately 2 sec on average). 3) Reach the target point and obtain a measurement with the pole tip as it lands directly on the target. 4) Continue walking along the designed trajectory in the walking stick mode until the endpoint is reached while maneuvering the pole as described for approximately 1 min. 5) Reverse the starting point and the ending point and

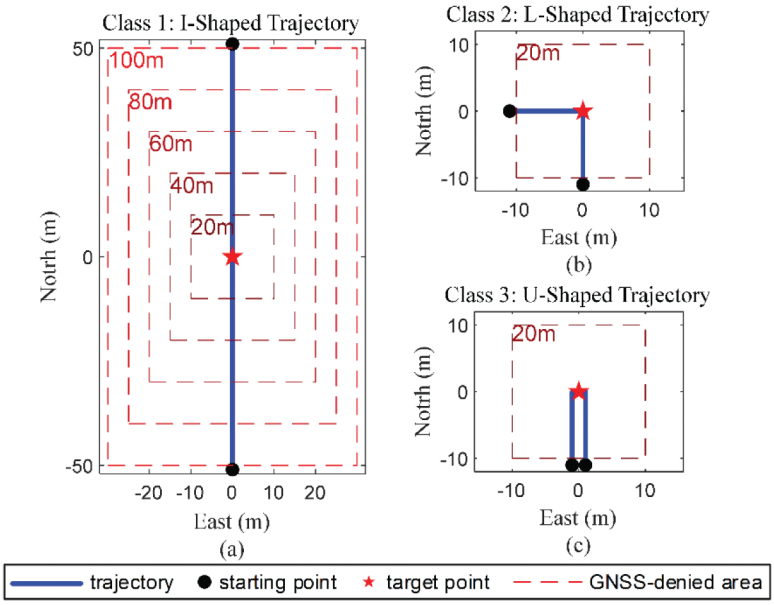

FIGURE 5 Diagram of the designed trajectories with three different shapes through the GNSS-denied area

TABLE 1
Data Processing Cases Collected for this Study

Index	Shape of trajectory	GNSS gap length	Repetitions	Result Group 1	Result Group 2
Case 1	I shape	100 m	30	•	
Case 2	I shape	80 m	30	•	
Case 3	I shape	60 m	30	•	
Case 4	I shape	40 m	30	•	
Case 5	I shape	20 m	30	•	•
Case 6	L shape	20 m	19		•
Case 7	U shape	20 m	17		•

Note: The black dots in the two final columns means the corresponding case is added in the Result Group.

walk along the reverse trajectory while taking another set of measurements. NB: maneuvering the pole at the ending and starting points was carried out by shifting it so that the end of the pole moved from one arbitrary point to another with the tip fixed at a point on the ground. To perform these tests, the surveyor walked back and forth 30 times and obtained measurements of the target point along the 100-meter I-shaped trajectory. These data were processed with different simulated GNSS gap lengths in Cases 1 to 5 (Group 1) to investigate the influence of trajectory distances in GNSS-denied areas. L-shaped and U-shaped trajectory datasets were collected similarly based on 19 and 17 repetitions, respectively, in Cases 5 to 7 (Group 2) to investigate the influence of the trajectory shapes using the same 20-meter GNSS gap length. The specifications of these data processing cases are listed in Table 1.

3.2 | Effects of LA-ZUPT and Smoothing

To investigate the benefits and limitations of LA-ZUPT in INS-based EKF and RTS smoothing, we considered Case 1 which is a typical example with an

I-shaped trajectory and a 100 m GNSS gap (i.e., a 140 s GNSS outage) using the ground truth from the INS/RTK system as a reference. We note that the INS was fully initialized at the beginning. The test data were processed in the following four modes:

1) INS/RTK filtering (EKF) without LA-ZUPTs
2) INS/RTK filtering (EKF) with LA-ZUPTs
3) INS/RTK smoothing (RTS) without LA-ZUPTs
4) INS/RTK smoothing (RTS) with LA-ZUPTs

The findings shown in Figure 6 present the results of navigation with the inertial-aided positioning pole as described in the example and post-processed in one of the aforementioned four modes. The GNSS outage began at 5 s and ended at 145 s. The two subfigures are the error plots of the filtering and smoothing results both with and without LA-ZUPT. Each mode shows the plots of the position, velocity, roll and pitch, and heading errors. The errors in different directions are distinguished by colors.

The findings shown in Figure 6a documenting EKF performance with and without LA-ZUPT reveal that 1) the pure INS drift is significant during the GNSS outage in the absence of any external measurements. However, the use of RTK positioning for CUPT in the INS-based EKF at the ending point reduced the INS errors to some extent, except for the heading error due to insufficient pole movement at the end; and 2) LA-ZUPT during GNSS outage can greatly reduce the velocity and horizontal attitude errors and can thus restrict the drift of INS position errors. While this is slower than INS without LA-ZUPT, it provides no help with respect to heading error estimations. The estimated heading had a significant step when the EKF received the first position observation from the GNSS RTK receiver after the GNSS outage; this may be due to the fake observability introduced by LA-ZUPT and the EKF's pessimistic prediction update of the P matrix based on the pessimistic IMU error model parameter. This result indicated that more parameter tuning work will be needed to build a consistent IMU error model.

The performance of the RTS smoothing with and without LA-ZUPT presented in Figure 6b reveals that 1) although RTS smoothing may reduce the INS-alone positioning errors from hundreds of meters to several meters, the addition of LA-ZUPT with the INS remains significant and highly promising with respect to further improvements in INS positioning accuracy to the decimeter level; and 2) after LA-ZUPT and RTS smoothing, the largest attitude error appears in the heading estimate, which appears to drift over time. Correspondingly, the positioning error is largest in the west-east direction. This is the transverse direction of the trajectory which is vulnerable to heading error; the same is true for the velocity error. Collectively, these findings indicate that heading error is the dominant source of error and that it is possible to obtain superior positioning results by improving the heading accuracy at the beginning and end of the GNSS outage.

In conclusion, the low-cost INS benefits significantly from LA-ZUPT in areas of GNSS outages as well as from RTS smoothing that fully exploits the RTK positioning at the starting and ending points. Since the position error appears to be closely related to the heading error, the latter should be considered a critical issue to be addressed in the proposed RTK extension solution.

Maneuvers performed at the starting and ending points can mitigate the impact of the heading error and facilitate the convergence of the heading estimates using RTK positioning updates, as discussed in Section 2.2. To explore the positioning

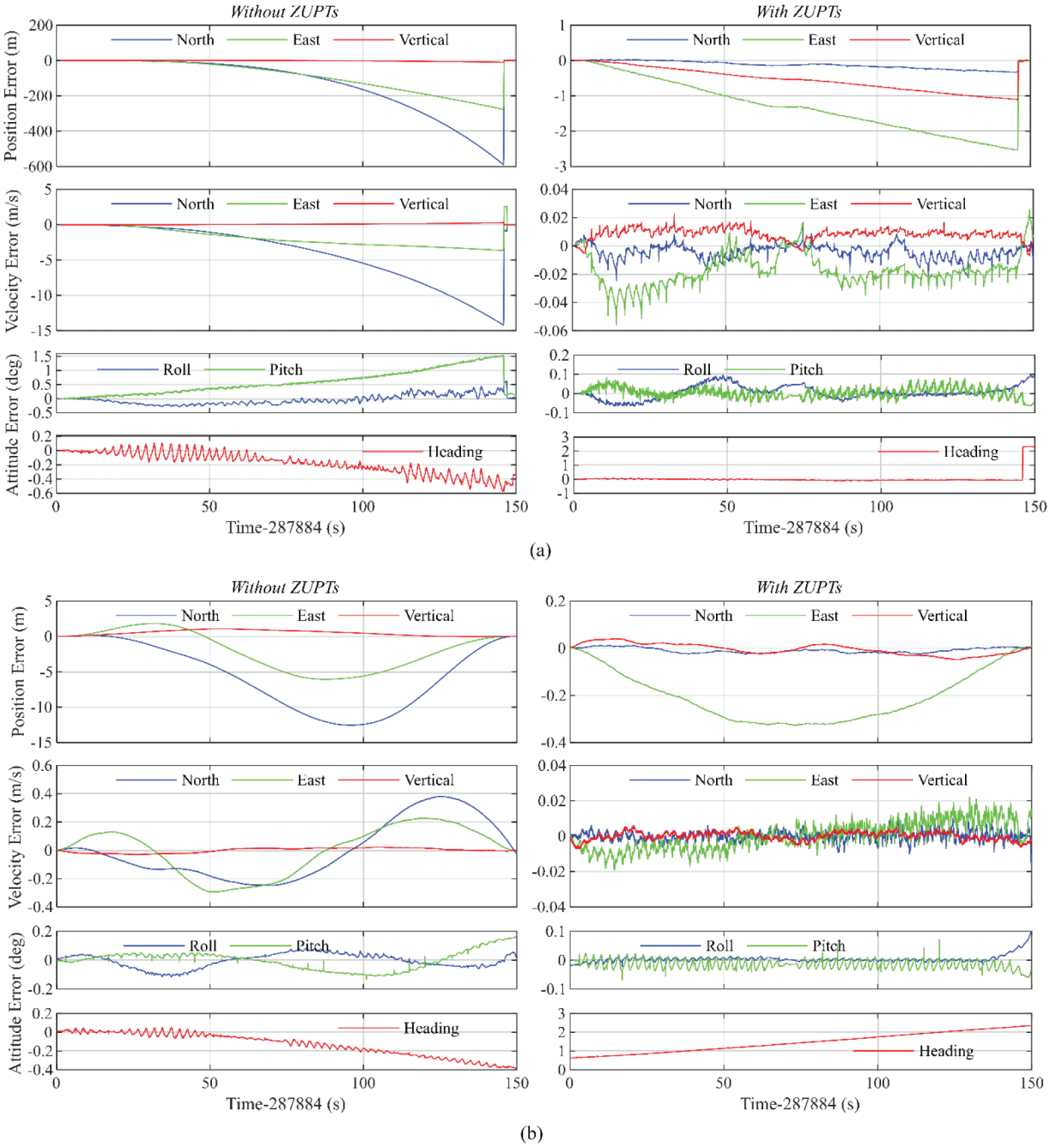

FIGURE 6 Comparison of the INS navigation errors using four different data processing modes. Assistance for RTK positioning is available at the beginning and end for only a few seconds.

performance of the aided INS with improved headings, several minutes of pole maneuvering at the ending point were added to the data processing. The errors associated with the estimated results are shown in Figure 7. As shown, the heading error is further reduced in the EKF and RTS; the maximum position error of the INS after RTS smoothing is reduced from 0.3 m to 0.15 m, confirming the link between the heading error and transverse positioning error in the smoothing result. These findings indicate that the heading error is the dominant source of error associated with transverse positioning. Thus, it will be necessary to address the drift heading issue by making the heading converge with the help of GNSS RTK positioning from outside the GNSS-denied area.

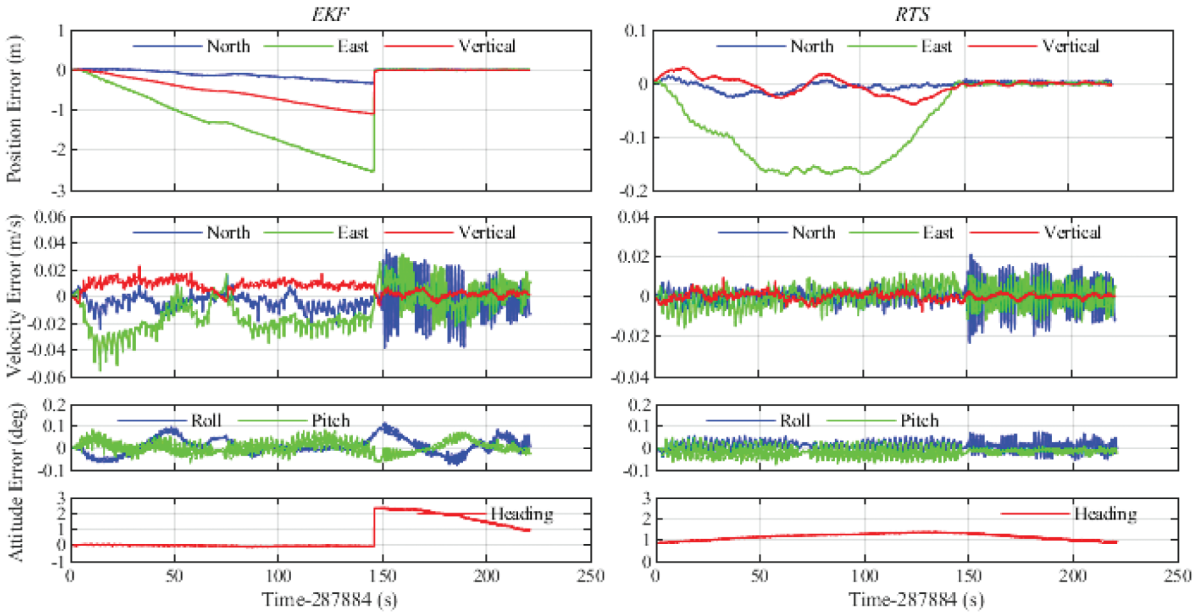

FIGURE 7 INS result aided by LA-ZUPT and RTK positioning with heading convergence at the end. The assistance of RTK positioning is available not only at the beginning but also at the end. Sufficient maneuvering will be required to facilitate the convergence of the INS heading.

3.3 | Positioning Performance Analysis

As described in Section 3.2, the INS error is reduced by LA-ZUPT, while the position and heading constraints on both sides of the GNSS outage region depend on RTS smoothing. In these cases, the shape of the trajectory (i.e., the geometric constraints discussed in Section 2.2) and the GNSS gap length are expected to be the two main factors that affect the performance of the RTK extension solution. In this section, we will investigate the cases assigned to Group 1 and Group 2 using the aforementioned surveyed reference truth coordinates of the target points to evaluate the positioning performance of the proposed RTK extension solution.

3.3.1 | Performance with Different GNSS Gap Lengths

Since the GNSS gap length is considered an important factor that influences the positioning performance, Cases 1–5 in Group 1 with GNSS gap lengths varying from 100 m to 20 m (as described in Figure 5) were investigated. The positioning errors are plotted in Figure 8 and the overall 3D positioning RMSE in are shown in Figure 9. The corresponding statistical values are listed in Table 2.

As shown in Table 2 and Figure 8, the position errors have similar characteristics to those shown in the plots in Figure 6 and Figure 7. Some points with larger position errors are distributed in the transverse direction (i.e., toward the east) compared to other directions (i.e., the heading and height directions), which can be easily affected by the estimated heading drift. By contrast, the height determination is much more accurate than the horizontal position and can maintain centimeter-level accuracy regardless of the 100-meter GNSS gap. Moreover, the overall means of the position errors in Cases 1–5 are smaller than 0.015 m, indicating that, although it exhibits a discrete distribution, the position errors in the transverse direction remain unbiased.

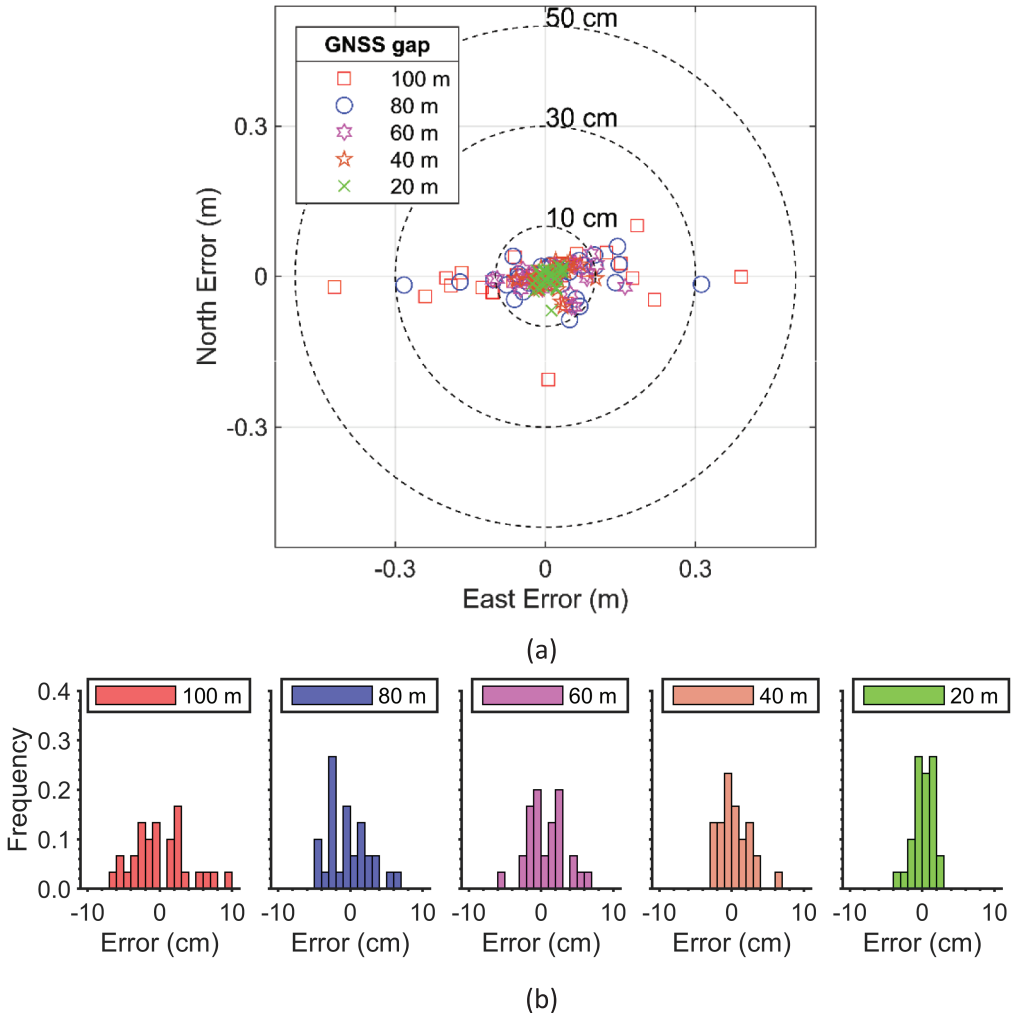

FIGURE 8 The positioning error of the proposed RTK extension solution in Cases 1–5

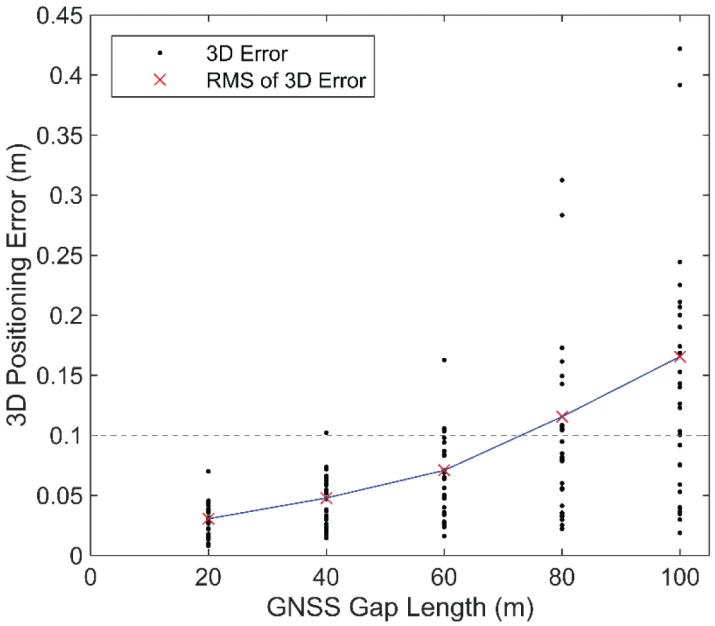

FIGURE 9 Correlation of positioning accuracy with GNSS gap length

The findings shown in Figure 9 document the correlation of the 3D positioning accuracy with the GNSS gap length. As the length of the GNSS gap is reduced, the positioning accuracy indicated by the RMSE improves in all three dimensions. When the distance is shorter than 60 m, for example, in Cases 3–5, the positioning accuracy is at the centimeter level based on the RMSE. Furthermore, in Case 5 (with a 20-meter GNSS gap length), the pole tip maximum 3D positioning error is less than 7 cm, with an RMSE of less than 2 cm; these values approximate the real RTK survey accuracy. These test results revealed that the proposed RTK extension solution used to assess a GNSS gap length of fewer than 60 meters will reach centimeter-level positioning accuracy. Thus, this technology will be feasible in a variety of scenarios, for example, surveys carried out in small buildings or under bridges, overpasses, or dense tree canopies.

3.3.2 | *Performance with Different Trajectory Shapes*

Considering the limited availability of GNSS-friendly spots that are close to a given target point, the influence of the location of the starting point and the ending point was investigated. In Group 2, Cases 5–7 with typical I-, L-, and U-shaped trajectories were tested. The I-shaped trajectory ostensibly provides the best constraint on the position error in the transverse direction as well as on the heading error. By contrast, the L-shaped and U-shaped trajectories are more flexible and remain applicable in a variety of GNSS-denied scenarios.

The horizontal position error distributions of Cases 5, 6, and 7 are shown in Table 3 and Figure 10. The results show that 1) the horizontal position error is generally more biased in Cases 6–7 than Case 5; 2) Case 7, with the U-shaped trajectory, performs the least effectively with a discrete distribution, which can be explained based on the weaker geometric constraints with respect to position and heading. To envision this more clearly, the control points can be compared to rivets, and the INS trajectory can be compared to a hinge with one end anchored by a rivet. Execution of RTS smoothing is analogous to pulling one end of the hinge to make sure that it is anchored by the other rivet. The smoothing process that leads to the obvious directional positioning errors at the middle points of

TABLE 2.
Positioning Errors of the Target Point Measured by the Inertial Pole for Different GNSS Gap Lengths

Unit: meters	Case 1 (100 m)			Case 2 (80 m)			Case 3 (60 m)			Case 4 (40 m)			Case 5 (20 m)		
	N	E	H	N	E	H	N	E	H	N	E	H	N	E	H
RMSE	0.049	0.154	0.038	0.031	0.108	0.029	0.024	0.061	0.026	0.022	0.037	0.021	0.019	0.019	0.014
MEAN	–0.005	–0.008	0.000	–0.002	0.015	–0.003	–0.004	0.014	0.007	–0.002	0.011	0.003	–0.004	0.007	0.001
MAX	0.101	0.391	0.094	0.059	0.312	0.061	0.045	0.159	0.061	0.031	0.101	0.063	0.021	0.035	0.027

Note: N denotes north, E denotes east and H denotes height.

TABLE 3.
Positioning Errors of the Target Point Measured by the Inertial Pole with Different Trajectory Shapes

Unit: meters	Case 5 (I-shaped)			Case 6 (L-shaped)			Case 7 (U-shaped)		
	N	E	H	N	E	H	N	E	H
RMSE	0.019	0.019	0.014	0.053	0.056	0.026	0.038	0.111	0.047
MEAN	-0.004	0.007	0.001	0.033	-0.049	0.021	-0.017	-0.083	-0.014
MAX	0.021	0.035	0.027	0.11	0.094	0.046	0.082	0.261	0.106

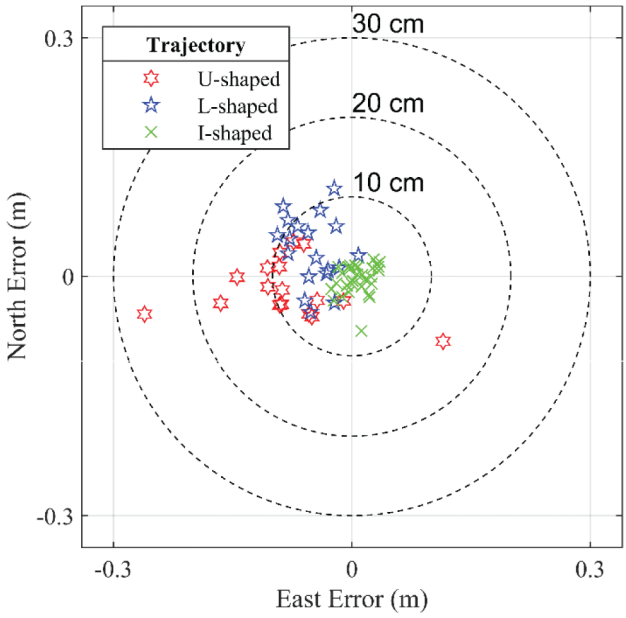

FIGURE 10 Horizontal positioning error distribution in Cases 5–7

the L- and U-shaped INS trajectories is similar to what transpires as part of a hinge-pulling process.

Interestingly, for Case 6, with an L-shaped trajectory, the maximum 2D position error is still less than 12 cm, and the RMSE remains less than 6 cm in the three position dimensions. Thus, this may remain feasible and suitable for specific surveying needs.

3.3.3 | *Performance with a Back-and-Forth Combination*

Given that the horizontal position errors of Cases 1–5 follow an axisymmetric distribution, will be beneficial to average the two adjacent positioning results from the same target point measured by going back and forth multiple times along the I-shaped trajectory. Thus, the 30 measurements are divided into 15 groups, in which two position measurements are used to complete a back-and-forth loop and the average of forward and reverse measurements was used for higher accuracy and robustness.

The findings shown in Figure 11 and Table 4 reveal a greater than 40% reduction in the overall position error in terms of RMSE and maximum error. In Cases 3–5 with GNSS gaps no greater than 60 m, the RMSE was approximately 5 cm and the maximum error did not exceed 10 cm. This result suggests that more accurate and robust results can be obtained by averaging the back-and-forth measurements while sacrificing half of the operational efficiency.

4 | DISCUSSION

To show the correlation of positioning accuracy with walking distance in GNSS-denied areas, a compensatory experiment was added to explore the nature of the positioning error along the I-shaped trajectory. The result of the tilted RTK solution was regarded as the ground truth and the positioning errors of each ground point in contact with the pole tip at each step were calculated. The distance

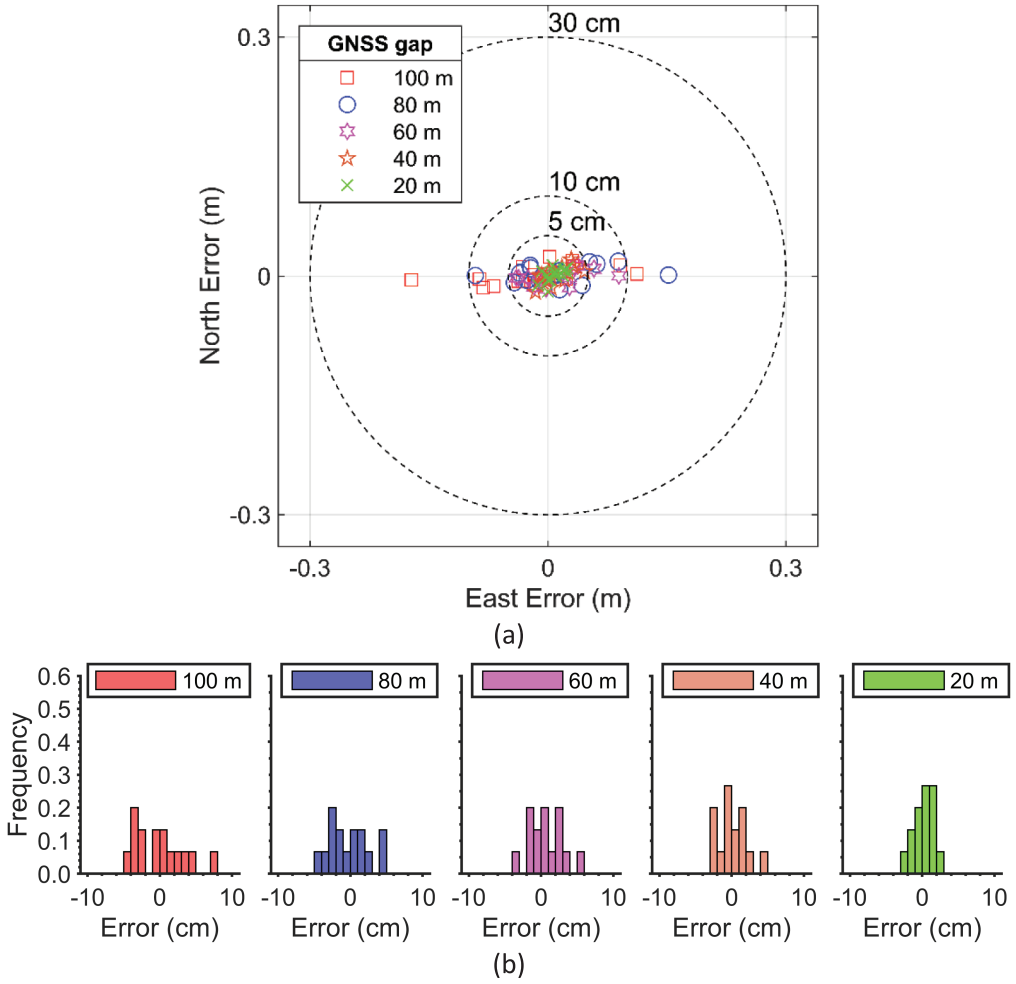

FIGURE 11 The positioning error of the RTK extension solution with a back-and-forth combination in Cases 1–5

TABLE 4.
Positioning Errors of the Target Point Measured by the Inertial Pole with the Back-and-Forth Combination

Unit: meters	Case 1 (100 m)			Case 2 (80 m)			Case 3 (60 m)			Case 4 (40 m)			Case 5 (20 m)		
	N	E	H	N	E	H	N	E	H	N	E	H	N	E	H
RMSE	0.011	0.071	0.028	0.011	0.059	0.019	0.008	0.036	0.015	0.011	0.02	0.013	0.008	0.014	0.009
MEAN	0.002	–0.017	–0.014	0.003	0.012	–0.011	–0.001	0.01	0.003	0.002	0.009	0.000	0.001	0.008	0.001
MAX	0.023	0.112	0.024	0.018	0.152	0.013	0.013	0.089	0.026	0.02	0.046	0.025	0.013	0.025	0.013

along the 100-meter trajectory was divided into 20 bins; the corresponding statistical results are shown in Figure 13.

The findings shown in Figure 13 reveal that while the vertical positioning accuracy is not vulnerable to changes in the walking distance in the GNSS-denied area, this factor has a profound impact on positioning accuracy in the east direction. This is likely because the heading angle drifts significantly and has an effect on plane positioning, while the roll and pitch angle errors are fully observable and controlled by LA-ZUPT. In addition, the statistical results also indicated that the three-dimensional positioning RMSE of the points with the greatest distance to spots where GNSS is available is the largest overall; thus, it is feasible to choose the middle point of the trajectory as the target point to evaluate the positioning performance.

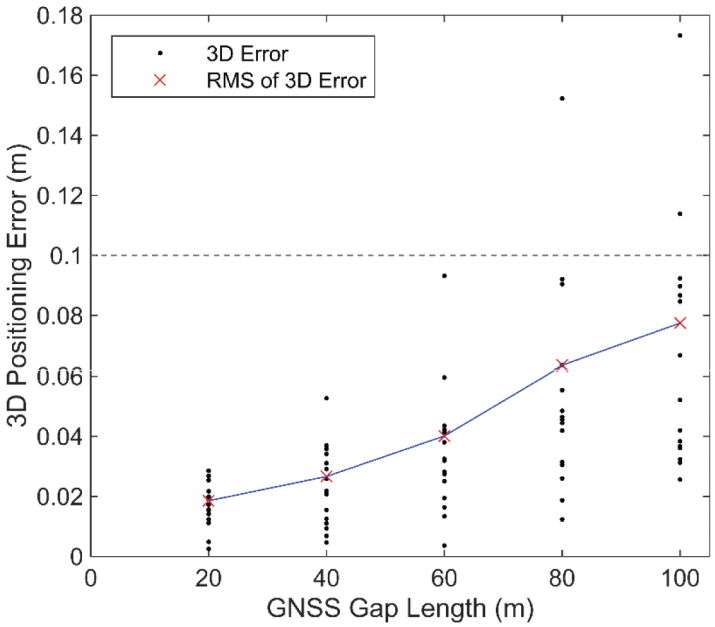

FIGURE 12 Correlation of positioning accuracy with GNSS gap length

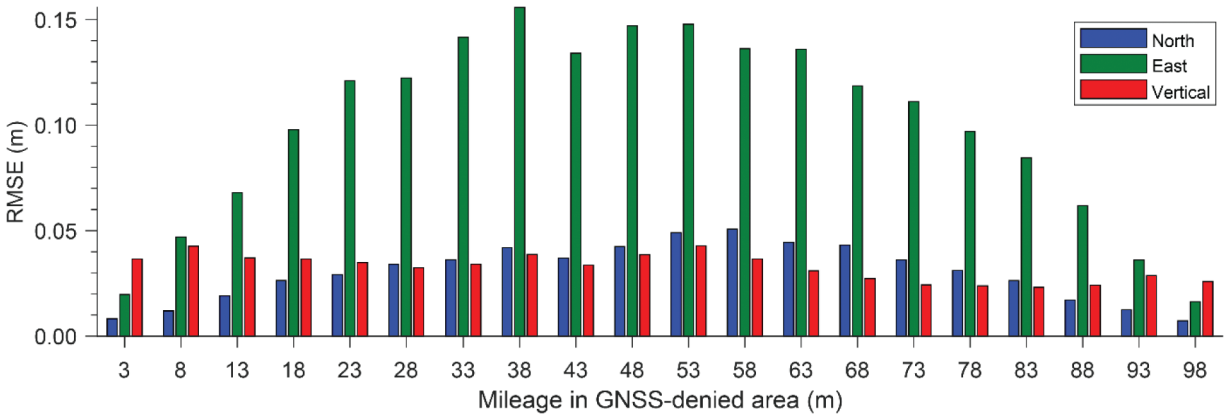

FIGURE 13 Correlation of positioning accuracy with walking distance in the GNSS-denied area

5 | CONCLUSION

To extend RTK survey capabilities to GNSS-denied areas at a reasonable cost, we have proposed an RTK extension solution using a low-cost inertial-aided positioning pole that can be operated as a walking stick. The solution uses an inexpensive MEMS IMU fixed on the RTK survey pole that performs the inertial navigation aided by 1) LA-ZUPT when the pole tip touches the ground on a regular basis. This effectively reduces the velocity and the horizontal attitude error and significantly limits the position drift; 2) the CUPT provided by RTK positioning at both the starting and ending points around the target point that is processed by the EKF and RTS smoothing algorithms and provides strict geometric constraints for the INS position drift; and 3) an accurate heading constraint at the starting and ending points that is obtained by enhancing the heading observability through sufficient maneuvering of the pole with the RTK positioning update. When considering the availability of open-sky areas around the target point, i.e., the geometry and distribution of the starting and ending point, different lengths and shapes of the trajectories, including

those that are I, L, or U-shaped, were tested as part of a comprehensive validation of the feasibility and performance of this RTK survey-extending solution. The experimental results with multiple datasets revealed that centimeter-level positioning can be achieved using I-shaped trajectories of under 40 m in length and L-shaped trajectories of 20 m as indicated by the RMSE. Similarly, we found that combining (i.e., averaging) the two positioning results measured along the back-and-forth I-shaped trajectories leads to a result that is more accurate and robust, with the RMSE and maximum error reduced by more than 40%. The proposed low-cost RTK extension solution using an inertial-aided positioning pole has been validated as feasible and can meet the requirements for extending the RTK survey capability to GNSS-denied areas over specific distances.

Future work will focus on additional improvements to the RTK extension solution, including 1) a thorough theoretical analysis of the INS error observability to optimize the hardware design, operation procedures, and algorithm parameters; 2) developing quality control for the multisensor integration algorithm and an integrity study of the entire system; and 3) replacement of the mechanical trigger by automatic detection based on the IMU data.

ACKNOWLEDGMENTS

We would like to thank Dr. Kuang Jian and Yu Li, who motivated us to consider the idea of ZUPT with lever-arm compensation, and Dr. Tisheng Zhang and Hailiang Tang for providing the GNSS/INS system (i.e., the *INS-Probe*) used in these experiments. The authors also gratefully acknowledge the research grant support provided by *The National Key Research and Development Program of China* (No. 2016YFB0502202) and *the National Natural Science Foundation of China* (41904019).

REFERENCES

Chen, Q., Niu, X., Zuo, L., Zhang, T., Xiao, F., Liu, Y., & Liu, J. (2018). A railway track geometry measuring trolley system based on aided INS. *Sensors (Basel)*, *18*(2), 538. https://doi.org/10.3390/s18020538

Chen, Q. J., Lin, H., Guo, R. N., & Niu, X. J. (2020). Rapid and accurate initial alignment of the low-cost MEMS IMU chip dedicated for tilted RTK receiver. *GPS Solutions*, *24*(4). https://doi.org/10.1007/s10291-020-01032-8

Chen, Q. J., Niu, X. J., Zhang, Q., & Cheng, Y. H. (2015). Railway track irregularity measuring by GNSS/INS integration. *NAVIGATION*, *62*(1), 83–93. https://doi.org/10.1002/navi.78

Chen, Q. J., Zhang, Q., Niu, X. J., & Wang, Y. (2019). Positioning accuracy of a pipeline surveying system based on MEMS IMU and odometer: Case study. *IEEE Access*, *7*, 104453–104461. https://doi.org/10.1109/Access.2019.2931748

Chowdhury, M. S., & Abdel-Hafez, M. F. (2016). Pipeline inspection gauge position estimation using inertial measurement unit, odometer, and a set of reference stations. *ASCE-ASME Journal of Risk and Uncertainty in Engineering Systems, Part B, Mechanical Engineering*, *2*(2), 021001–021001. https://doi.org/10.1115/1.4030945

El-Sheimy, N., & Youssef, A. (2020). Inertial sensors technologies for navigation applications: State of the art and future trends. *Satellite Navigation*, *1*(1), 2. https://doi.org/10.1186/s43020-019-0001-5

Feliz Alonso, R., Zalama Casanova, E., & Gómez García-Bermejo, J. (2009). Pedestrian tracking using inertial sensors. *Journal of Physical Agents*, *3*(1), 35–42. https://doi.org/10.14198/JoPha.2009.3.1.05

Foxlin, E. (2005). Pedestrian tracking with shoe-mounted inertial sensors. *IEEE Computer Graphics and Applications*, *25*(6), 38–46. https://doi.org/10.1109/mcg.2005.140

Gao, Z. Z., Ge, M. R., Li, Y., Shen, W. B., Zhang, H. P., & Schuh, H. (2018). Railway irregularity measuring using Rauch-Tung-Striebel smoothed multi-sensors fusion system: Quad-GNSS ppp, IMU, odometer, and track gauge. *GPS Solutions*, *22*(2), 14, Article 36. https://doi.org/10.1007/s10291-018-0702-5

Guan, L., Cong, X., Zhang, Q., Liu, F., Gao, Y., An, W., & Noureldin, A. (2020). A comprehensive review of micro-inertial measurement unit based intelligent PIG multi-sensor fusion technologies for small-diameter pipeline surveying. *Micromachines (Basel)*, *11*(9), Article 840. https://doi.org/10.3390/mi11090840

Hein, G. W. (2020). Status, perspectives and trends of satellite navigation. *Satellite Navigation*, *1*(1), 22. https://doi.org/10.1186/s43020-020-00023-x

Hong, S. P., Lee, M. H., Chun, H. H., Kwon, S. H., & Speyer, J. L. (2005). Observability of error states in GPS/INS integration. *IEEE Transactions on Vehicular Technology*, *54*(2), 731–743. https://doi.org/10.1109/Tvt.2004.841540

Luo, X., Schaufler, S., Carrera, M., & Celebi, I. (2018, May 6–11). *High-precision RTK positioning with calibration-free tilt compensation.* International Federation of Surveyors (FIG) Congress 2018, Istanbul, Turkey. http://fig.net/resources/proceedings/fig_proceedings/fig2018/papers/ts04e/TS04E_luo_schaufler_et_al_9407.pdf

Maybeck, P. S. (1979). *Stochastic models, estimation and control*. Academic Press. https://www.elsevier.com/books/stochastic-models-estimation-and-control/maybeck/978-0-12-480703-7

Niu, X. J., Li, Y., Kuang, J., & Zhang, P. (2019). Data fusion of dual foot-mounted IMU for pedestrian navigation. *IEEE Sensors Journal*, *19*(12), 4577–4584. https://doi.org/10.1109/Jsen.2019.2902422

Rauch, H. E., Tung, F., & Striebel, C. T. (1965). Maximum likelihood estimates of linear dynamic systems. *AIAA Journal*, *3*(8), 1445–1450. https://doi.org/10.2514/3.3166

Ren, M., Pan, K., Liu, Y., Guo, H., Zhang, X., & Wang, P. (2016). A novel pedestrian navigation algorithm for a foot-mounted inertial-sensor-based system. *Sensors (Basel)*, *16*(1), 139. https://doi.org/10.3390/s16010139

Scherzinger, B. (2005). *Walking stick navigator for position determination* (US Patent No. 6853909B2). U.S. Patent and Trademark Office. https://www.freepatentsonline.com/y2009/0024325.html

Scherzinger, B. (2009). *AINS enhanced survey instrument* (US Patent No. 20090024325A1). U.S. Patent and Trademark Office. https://www.freepatentsonline.com/y2009/0024325.html

Schwarz, K. P. (1983). Inertial surveying and geodesy. *Reviews of Geophysics*, *21*(4), 878–890. https://doi.org/10.1029/RG021i004p00878

Shin, E.-H. (2005). *Estimation techniques for low-cost inertial navigation* [Unpublished doctoral thesis]. University of Calgary. http://dx.doi.org/10.11575/PRISM/2386

Teunissen, P., & Montenbruck, O. (2017). *Springer handbook of global navigation satellite systems* (1st ed. 2017). Springer International Publishing. https://doi.org/10.1007/978-3-319-42928-1

How to cite this article: Lai, C., Guo, R., Chen, Q., & Niu, X. (2023) Extending the real-time kinematics survey method to global navigation satellite system-denied areas using a low-cost inertial-aided positioning pole. *NAVIGATION, 70*(3). https://doi.org/10.33012/navi.584